EDGE ARTICLE

An ultrasensitive 2,4,6-trinitrophenol nanofluidic sensor inspired by olfactory sensory neurons in sniffer dogs†

Xin Li,[af] Zhanfang Liu,[b] Linsen Yang,[a] Shengyang Zhou,[a] Yongchao Qian,[a] Yuge Wu,[af] Zidi Yan,[af] Zhehua Zhang,[af] Tingyang Li,[af] Qingchen Wang,[af] Congcong Zhu,*[a] Xiang-Yu Kong [ID] [acdf] and Liping Wen [ID] *[acdef]

Explosives, as high-energy materials, could generate huge destructive explosions along with a massive release of energy. The regulatory or illegal transportation of explosives threatens the peace and stability worldwide. Among the many high-powered explosives, 2,4,6-trinitrophenol (TNP) is not only frequently used in many terrorist attacks, but also seriously jeopardizes environmental safety and human health. Hence, dependable methods for high-sensitivity, rapid and portable detection are desperately needed. Inspired by olfactory sensory neurons (OSNs) in sniffer dogs, we present a nanofluidic sensor for ultrasensitive TNP detection by *in situ* growing dense UiO-66-NH$_2$ layers on the surface of anodic aluminum oxide (AAO) nanochannels. TNP could be specifically captured by UiO-66-NH$_2$ of the sensor through charge transfer to form Meisenheimer complexes, which cause the ionic current change. The TNP concentrations are quantitatively analyzed by monitoring the changed ionic current. And the detection range is from 10^{-14} to 10^{-10} g mL^{-1} with a limit of detection as low as 6.5×10^{-16} g mL^{-1}, which is far beyond those of the state-of-the-art sensors. This work provides a novel strategy for ultrasensitive detection of TNP as well as other explosives, which opens new and promising routes to various breakthroughs in the fields of homeland security, military applications, security inspections and environmental monitoring.

Introduction

Explosives, as high-energy materials, are widely used in the fields of weapon systems, explosive forming, space applications and engineering blasting. Also, explosives have become the powerful weapon in terrorist attack that threaten peace and stability worldwide.[1–3] As a more powerful explosive than trinitrotoluene (TNT), 2,4,6-trinitrophenol (TNP) is a frequent ingredient in industrial explosives and is often used in many unexploded bombs and terrorist attacks around the world.[4,5] It not only causes enormous devastation, but also damages the human nervous system and internal organs, as a pollutant in the earth and water.[6,7] Hence, it is of utmost significance to invent a rapid and sensitive detection method for TNP.[8–11] Until now, a series of detection methods have been developed, including using animals, ion mobility spectrometry, surface-enhanced Raman spectroscopy, fluorescence quenching, colorimetry, mass spectrometry and so on. Their expensive cost and sophisticated pretreatment limit their wide application during in-field use.[12] Therefore, fabricating a sensor for TNP detection with portable and sensitive performance is a challenge that needs to be urgently addressed.

Nanofluidic sensors would be an ideal answer to the above challenges as a powerful tool with rapid, low-cost, portable and ultrasensitive advantages.[13–15] Among numerous nanofluidic devices, bioinspired solid-state nanochannels are widely used to achieve smart sensing of diverse targets because of their advantages of functionalization, adjustable size, high mechanical stability, and controllable shape.[16–19] After targets are captured by the recognition element, the physicochemical properties (surface charge, wettability and steric hindrance) of nanochannels would be changed and significantly presented *via* transmembrane ionic current.[17] Bioinspired nanofluidic sensors have been demonstrated for an extensive range of

[a] *CAS Key Laboratory of Bio-inspired Materials and Interfacial Science, Technical Institute of Physics and Chemistry, Chinese Academy of Sciences, Beijing 100190, P. R. China. E-mail: zhucongcong17@mails.ucas.ac.cn; wen@mail.ipc.ac.cn*

[b] *Institute of Forensic Science, Ministry of Public Security, Beijing 100038, P. R. China*

[c] *Suzhou Institute for Advanced Research, University of Science and Technology of China, Suzhou, Jiangsu 215123, China*

[d] *School of Chemistry and Materials Science, University of Science and Technology of China, Hefei, Anhui 230026, P. R. China*

[e] *Qingdao Institute of Bioenergy and Bioprocess Technology, Chinese Academy of Sciences, Qingdao, 266101, P. R. China*

[f] *School of Future Technology, University of Chinese Academy of Sciences, Beijing 100049, P. R. China*

† Electronic supplementary information (ESI) available. See DOI: https://doi.org/10.1039/d4sc05493h

detection applications, including ions,[20–22] gas molecules,[23,24] small molecules,[25–27] biomolecules[28–31] and cells.[32,33] Recently, chemical modification on the outer-surface of nanochannels has provided an alternative strategy for functional layer construction to recognize the target sensitively. Meanwhile, tunable pore metrics, structural diversity and rich functionality are also the key parameters for nanofluidic sensing performances. Metal–organic framework (MOF) materials, which have a large surface area, high porosity and abundant functional sites, are the prime candidates for designing nanofluidic sensors.[8] Combining MOFs with nanochannels would provide an advanced TNP detection strategy.

Here, we demonstrate a biomimetic olfactory nanofluidic sensor for ultrasensitive TNP detection. Inspired by the dog's sensory neurons in the acute olfactory system, a TNP-responsive nanofluidic sensor (AAO@UiO-66-NH$_2$) is constructed by growing dense MOF (UiO-66-NH$_2$) layers *in situ* on the outer surface of anodic aluminum oxide. When TNP molecules are specifically captured by the amino groups of AAO@UiO-66-NH$_2$ through charge transfer and hydrogen bonding interaction,[2,34–36] the surface charge density and steric hindrance of the nanochannels would be regulated by the specific molecular recognition, which governs the ion transport behaviors. The concentrations of TNP are quantitatively analyzed by monitoring the changed ionic current, and the concentration range of TNP is from 1×10^{-14} to 1×10^{-10} g mL^{-1}. The nanofluidic sensor has an ultra-low detection limit of 6.5×10^{-16} g mL^{-1} which outperforms that of reported detection methods. This portable sensor is suitable for rapid quantitative analysis for strictly supervising TNP as well as other hazardous explosives to effectively lower the disastrous threat of terrorism.

Results and discussion

Fabrication of the nanofluidic sensor

"We see the world, dogs can smell it.[37]" Dogs have gotten honour in homeland security, military applications and security inspections due to their surpassing olfactory. Once the odour molecules bind to the corresponding receptor, G-proteins will be activated to generate cAMP molecules by the OSNs of the dog. The stepwise amplification process of the signal leads to ion transport through selective biological nanochannels, which realizes the conversion of chemical information to neural signals[38] (Scheme 1). Inspired by the dog's olfactory sensory neurons, we constructed a TNP-responsive nanofluidic sensor with excellent sensitivity and selectivity by AAO coupling UiO-66-NH$_2$ for TNP detection. As an electron-deficient
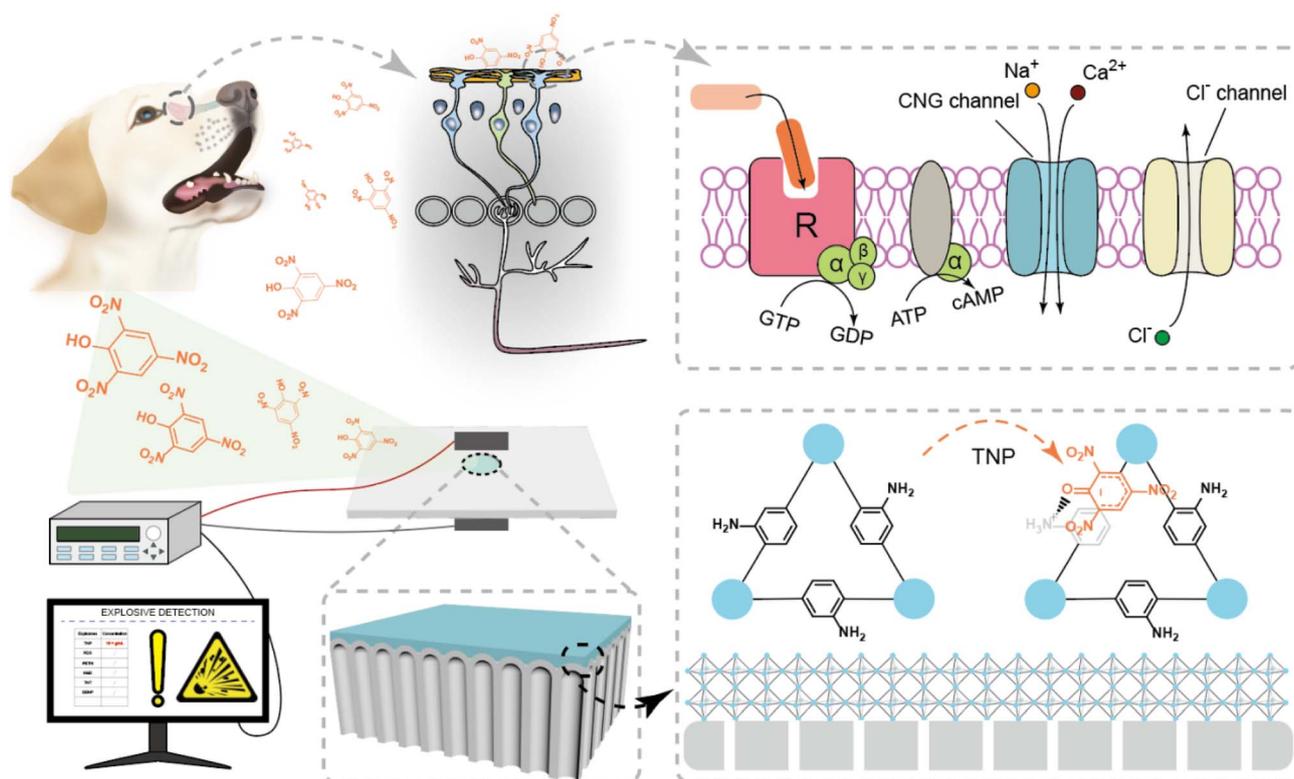
Scheme 1 The scheme of the OSNs-inspired nanofluidic sensor (AAO@UiO-66-NH$_2$) for TNP detection. TNP jeopardizes public safety and human health due to its extremely high explosive power and irreversible bodily harm. Large specific surface area in the maxilla turbinate and the hundreds of millions of olfactory receptors give dogs an extremely sensitive sense of smell. The detailed process is as follows, targets bind to their specific receptor, and the associated G-protein is activated which activates adenylyl cyclase and transforms adenosine triphosphate into adenosine 3′–5′-cyclic monophosphate (cAMP). The cAMP would open ion channels (a cyclic nucleotide-gated (CNG) channel), which leads to the occurrence of cation (Na$^+$ and Ca^{2+}) influx and action potentials are eventually generated. Inspired by the olfactory system, a biomimetic olfactory nanofluidic sensor based on *in situ* growth of UiO-66-NH$_2$ is fabricated to sensitively detect TNP.

nitroaromatic compound, TNP forms Meisenheimer complexes with electron-rich amino groups through charge-transfer complexing interactions due to the strong electron-withdrawing effect of the nitro group.[2,34–36] As a result, TNP molecules captured on AAO@UiO-66-NH$_2$ will regulate the ion transport through the confined interface of the nanofluidic sensor. The transmembrane ionic current will correspond to the concentration of TNP after the molecular recognition on AAO@UiO-66-NH$_2$.

The nanofluidic sensor is fabricated by *in situ* synthesis of a dense UiO-66-NH$_2$ layer on the barrier layer of AAO (Fig. 1a and S1†). First, (3-aminopropyl)triethoxysilane (APTES) molecules are modified on AAO as the covalent linker between the MOFs and AAO. During the growth process of UiO-66-NH$_2$ crystals, benzoic acid molecules are used to control the growth process and crystal size of UiO-66-NH$_2$, which is important to manufacture the dense and continuous MOF crystal layer. Compared with the AAO (Fig. 1b and S2†), the dense and continuous UiO-66-NH$_2$ layer is successfully grown on the outer surface of AAO (Fig. 1c). The thickness of UiO-66-NH$_2$ on the

barrier layer of AAO is about 580 nm. As shown in the cross-section image of AAO@UiO-66-NH$_2$ in Fig. 1d, the membrane is divided into two regions: the UiO-66-NH$_2$ layer and AAO channels. The diameter of the nanochannel of AAO is about 40–70 nm (Fig. S3†) and the diameter of sub-nanometer channels of AAO is about 1.3 nm.[32] X-ray photoelectron spectroscopy (XPS) demonstrates the modification process by the N 1s and Zr 3d typical peaks (Fig. 1e). The quantitative atomic analysis of XPS reveals the changes before and after modification (Fig. S4†). The decrease of Al (mole percentage) and increase of C and Zr prove the successful growth of UiO-66-NH$_2$ on AAO. The energy-dispersive spectroscopy (EDS) also confirms the successful modification compared with the unmodified nanochannels (Fig. S5–S7†). The roughness of the membrane also increases after the successful *in situ* growth of MOFs on the AAO (Fig. S8†). BET pore size distribution shows almost inherent pores with diameters of 6–7 Å and 1.06 nm in every single UiO-66-NH$_2$ crystal (Fig. 1f). The X-ray diffraction (XRD) patterns of AAO@UiO-66-NH$_2$ also prove the successful synthesis of UiO-66-NH$_2$ crystals (Fig. 1g).
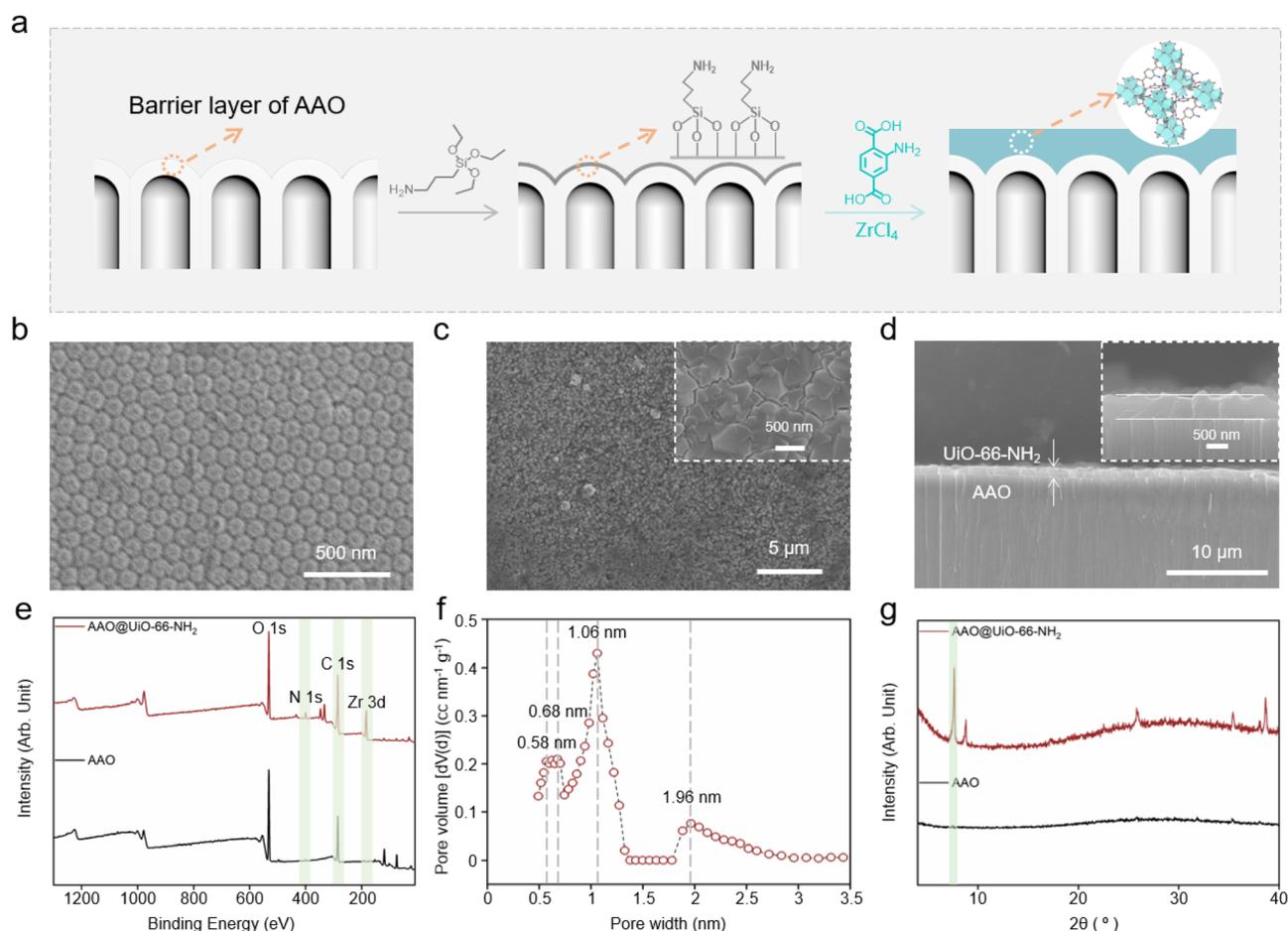

Fig. 1 Preparation and characterization of AAO@UiO-66-NH$_2$. (a) Scheme of the fabrication process of AAO@UiO-66-NH$_2$. (b) Top view scanning electron microscopy (SEM) images of AAO with a barrier. (c) Top view and (d) cross-section view of AAO@UiO-66-NH$_2$, indicating a continuous and dense UiO-66-NH$_2$ layer with a thickness of about 580 nm *in situ* growing on the AAO barrier. Inset: the amplified SEM images of the (c) top view and (d) cross-section view of AAO@UiO-66-NH$_2$. (e) X-ray photoelectron spectra (XPS) of AAO and AAO@UiO-66-NH$_2$. (f) Nominal pore size distributions of UiO-66-NH$_2$ calculated based on the N$_2$ adsorption/desorption isotherms. (g) X-ray diffraction (XRD) patterns of AAO and AAO@UiO-66-NH$_2$.

TNP detection by the nanofluidic sensor

Due to the strong electron-withdrawing effect of the three nitro groups, TNP with the electron-deficient aromatic ring could form strong interactions with electron-rich –NH$_2$ of UiO-66-NH$_2$ on the outer surface of AAO. The charge transfer from amino groups to aromatic rings leads to the formation of Meisenheimer complexes between TNP and the primary amino groups in UiO-66-NH$_2$ (Fig. S9†). On the other hand, TNP is selectively adsorbed by UiO-66-NH$_2$ because the phenolic hydroxyl group of TNP strongly and selectively interacts with the Lewis base of UiO-66-NH$_2$ *via* hydrogen bonding interactions. Meanwhile, this combination between TNP and UiO-66-NH$_2$ would influence the ionic transport behavior, which in turn alters the transmembrane currents. The quantitative analysis of TNP is realized by establishing a functional relationship between the concentrations of TNP and currents. The ion signal is monitored by

using two Ag/AgCl electrodes and the obtained electrical signal could be visualized to represent the concentration of TNP (Fig. 2a and S10†). It's worth noting that the anode is placed on the MOF layer side and 0.1 M KCl is chosen as the electrolyte. In order to achieve the optimum capturing time, TNP is dropped on the MOF side and incubated for different times (10, 20, 30, 40, 50, 60, 90, 120, 180 seconds) at room temperature (Fig. 2b). The transmembrane current changed significantly in a very short period of time and reached a stable result within 180 seconds. As shown in Fig. 2c, the transmembrane currents decrease from 5.2 μA to 0.47 μA when UiO-66-NH$_2$ is grown on the outer surface of AAO. Nevertheless, the currents increase from 0.47 μA to 3.3 μA after AAO@UiO-66-NH$_2$ capturing TNP. The surface charge density (zeta potential) decreases from −33.5 to −3.1 mV after modifying MOFs and increases to −29.8 mV after capturing TNP, respectively (Fig. 2d). Furthermore, AAO@UiO-66-NH$_2$ is
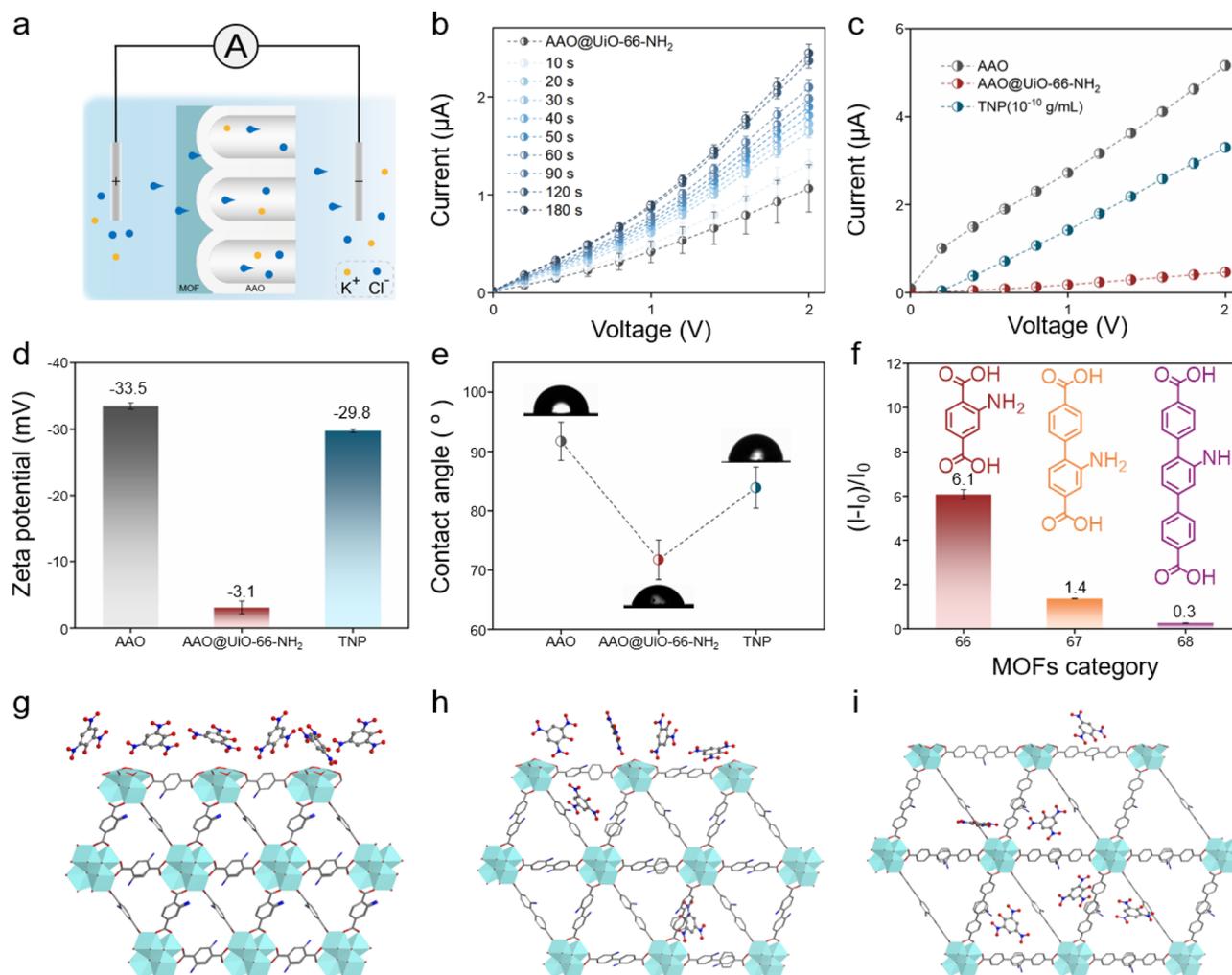

Fig. 2 The OSNs–inspired nanofluidic sensor (AAO@UiO-66-NH$_2$). (a) Scheme of the experimental setup for monitoring the ion current of the sensor. (b) The transmembrane currents of the nanofluidic sensor are obtained at different incubation times. (c) The ionic currents are obtained from AAO, AAO@UiO-66-NH$_2$ and TNP-responsive (TNP concentration: 10^{-10} g mL^{-1}). (d) Zeta potential and (e) contact angle (CA) of the AAO, AAO@UiO-66-NH$_2$ and TNP-responsive. (f) ($(I - I_0)/I_0$) relative change of ionic current *versus* different organic ligands of MOFs, where I stands for current at voltage +2 V after capturing TNP (concentration: 10^{-10} g mL^{-1}), and I_0 stands for the transmembrane current of the fabricated sensors. Different organic ligands have similar structures, distinguished by their lengths. (g–i) The calculation of micromolecular adsorption states on the three sensors.

observed to be more hydrophilic compared with unmodified AAO (Fig. 2e), which is attributed to the extra amino and carboxyl groups of UiO-66-NH$_2$ (contact angle (CA) from 91.7° to 71.7°). But after capturing TNP, AAO@UiO-66-NH$_2$ is more hydrophobic (CA from 71.7° to 83.9°) because of the extra benzene ring and nitro groups of TNP. The transmembrane current reduces because of the reduced surface charge density and the increased steric hindrance. After capturing TNP, the Meisenheimer complexes are formed between AAO@UiO-66-NH$_2$ and TNP, and the zeta potential of AAO@UiO-66-NH$_2$ is significantly elevated, which enhances the surface charge density and is reflected in the transmembrane current increase. UiO-66 without amino groups is also grown on the AAO using the same preparation strategy to prove the binding mechanism. After detecting the same concentration of TNP, the currents of AAO@UiO-66 barely

increase ($(I - I_0)/I_0 = 0.6$) compared with AAO@UiO-66-NH$_2$ ($(I - I_0)/I_0 = 6.1$) (Fig. S11†). In order to further reveal the mechanism of the effect on the nanochannel variations on the currents, two additional sensors (AAO@UiO-67-NH$_2$ and AAO@UiO-68-NH$_2$) are obtained by *in situ* growth of MOFs with similar structures but different organic ligand lengths. XPS demonstrates the successful growth of MOFs on AAO (Fig. S12–S14†). It is obviously observed that the currents of all three sensors increase after detecting TNP (Fig. S15†). However, the three sensors exhibit different sensitivities which could be distinguished by the relative change of currents. The relative change of currents of AAO@UiO-66-NH$_2$, AAO@UiO-67-NH$_2$ and AAO@UiO-68-NH$_2$ is 6.1, 1.4 and 0.3, respectively, which means that AAO@UiO-66-NH$_2$ has the highest sensitivity among the three sensors (Fig. 2f). This is attributed to the size-matched relationship between the
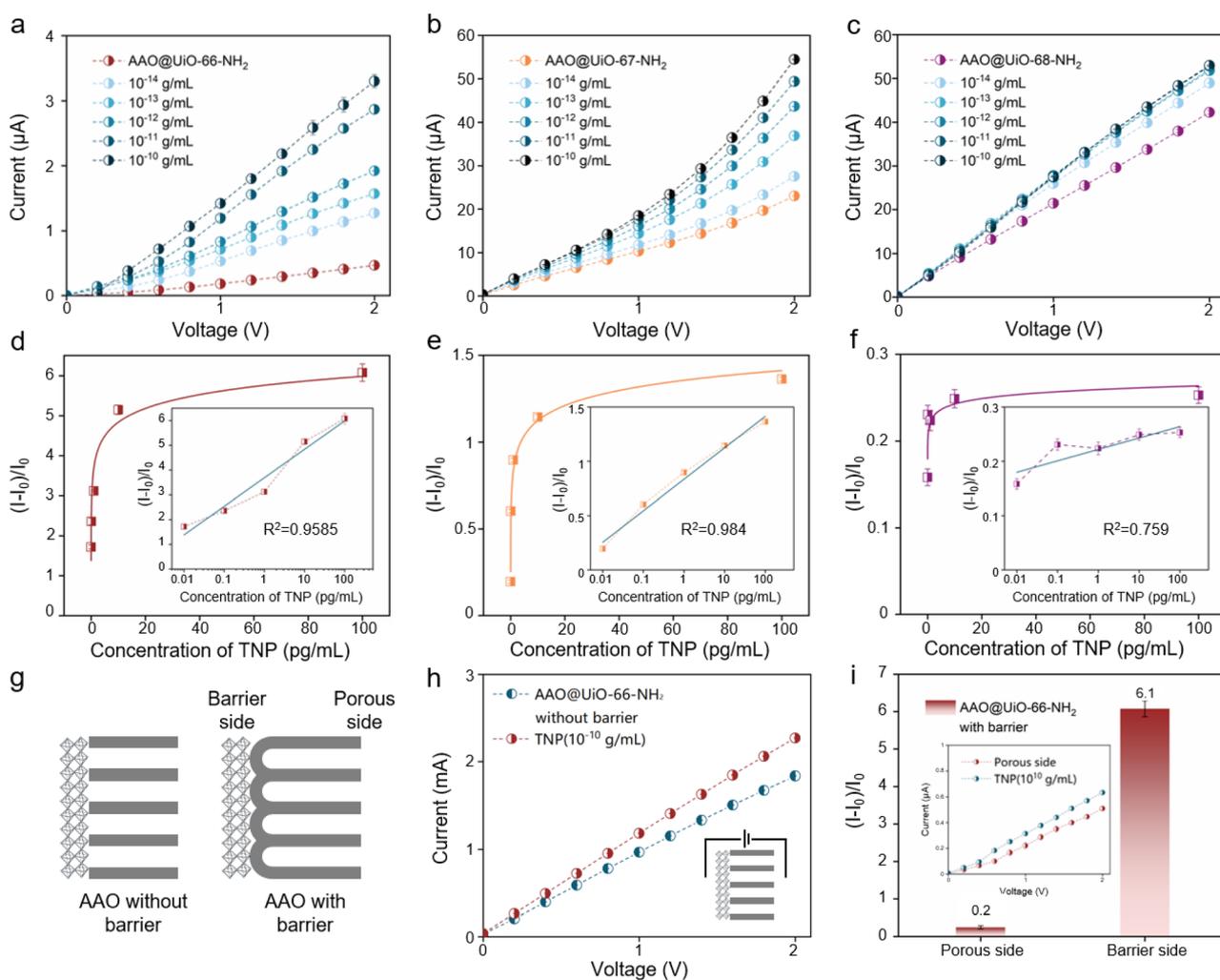

Fig. 3 The OSNs-inspired nanofluidic sensor for TNP detection. (a–c) I–V curves of the nanofluidic sensor with different concentrations of TNP using different sensors, AAO@UiO-66-NH$_2$ (a), AAO@UiO-67-NH$_2$ (b) and AAO@UiO-68-NH$_2$ (c). (d–f) The $((I - I_0)/I_0)$ relative change of current vs. different TNP concentrations of the three sensors, AAO@UiO-66-NH$_2$ (d), AAO@UiO-67-NH$_2$ (e) and AAO@UiO-68-NH$_2$ (f). Inset: linear calibration plot of $(I - I_0)/I_0$ vs. lg C, where I stands for current at voltage +2 V at different concentrations of TNP, I_0 stands for the transmembrane current of the fabricated sensors, and C denotes the TNP concentration. (g) Scheme of two AAO@UiO-66-NH$_2$ with and without a barrier layer. (h) I–V curves of AAO@UiO-66-NH$_2$ without a barrier layer for detecting the same concentration of TNP (10^{-10} g mL^{-1}). Inset: scheme of the experimental setup for monitoring the ion current of the sensor. (i) The $((I - I_0)/I_0)$ relative change of current of AAO@UiO-66-NH$_2$ with a barrier layer when incubating TNP on the porous side or barrier side. Inset: I–V curves of AAO@UiO-66-NH$_2$ with a barrier when incubating TNP on the porous side.

three MOFs and TNP. The spatial dimensions of TNP (Fig. S16†) are bigger than the pore limiting diameter (PLD) of UiO-66-NH$_2$ (3.7 Å) but smaller than the PLD of UiO-67-NH$_2$ (6.0 Å) and UiO-68-NH$_2$ (8.8 Å) (Table S1†). In this circumstance, it is difficult for TNP to enter UiO-66-NH$_2$ but it is adsorbed on the surface of UiO-66-NH$_2$ (Fig. 2g). The change of surface charge density dominates mass transport behavior compared to steric hindrance. But as for UiO-67-NH$_2$ and UiO-68-NH$_2$, TNP is able to enter the inter composition which leads to a combination of size and charge effects controlling ion transport behavior (Fig. 2h and i). Therefore, the transmembrane currents all exhibit an increase after detecting TNP due to charge enhancement, but the relative change of currents decreases sequentially with increasing length of the organic ligand because of steric hindrance.

TNP detection performance of the nanofluidic sensors

The detection performances of AAO@UiO-66-NH$_2$, AAO@UiO-67-NH$_2$ and AAO@UiO-68-NH$_2$ at different concentrations of TNP are verified to meet analysis needs. Different concentrations of TNP solution are used to assess their detection range and limit. The changed transmembrane currents of the three detection platforms could be obviously observed at different TNP concentrations. With the increase in TNP concentrations (10^{-14} to 10^{-10} g mL^{-1}), the currents of AAO@UiO-66-NH$_2$ increase from 1.3 to 3.3 μA (Fig. 3a) and the relative change of current increases from 1.7 to 6.1 μA (Fig. 3d). By plotting the $(I - I_0)/I_0$ at +2.0 V versus the logarithm of TNP concentration (lg C), the calibration curve is obtained. The curve equation is $y = 1.151 \times$ lg $C + 17.496$ ($R^2 = 0.9585$). The limit of detection (LOD) is 6.5×10^{-16} g mL^{-1} ($3S_0/K$) (where S_0 stands for deviation from the blank and K stands for the slope of the calibration curve). Also, the current of AAO@UiO-67-NH$_2$ increases from 27.5 to 54.5 μA (Fig. 3b) and the relative change of current increases from 0.2 to 1.4 μA (Fig. 3e), which is much smaller than that of AAO@UiO-66-NH$_2$. The curve equation is $y = 0.29 \times$ lg $C + 4.313$ ($R^2 = 0.984$). The limit of detection (LOD) is 2.0×10^{-15} g mL^{-1} ($3S_0/K$). But as for AAO@UiO-68-NH$_2$, the
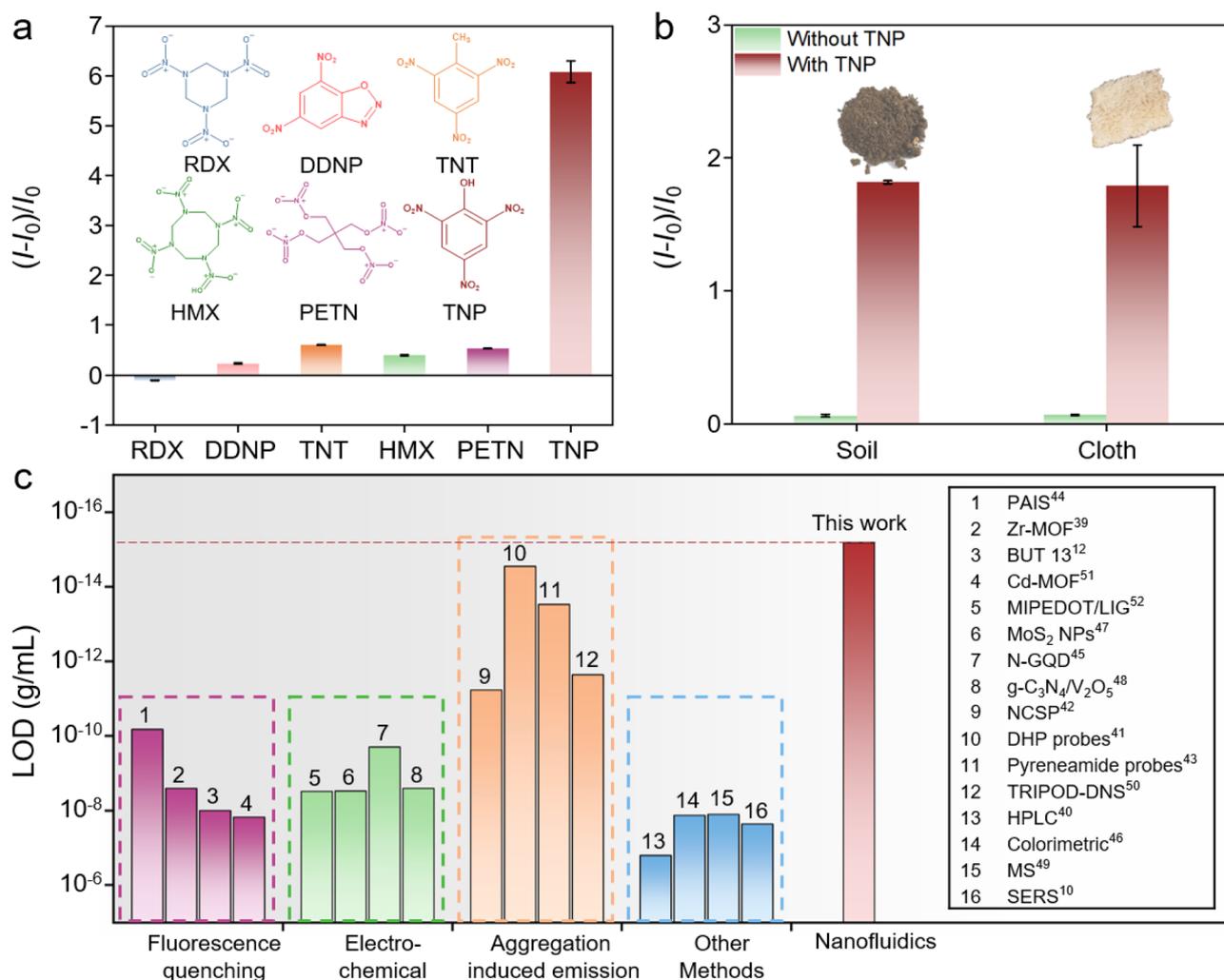

Fig. 4 Application viability of AAO@UiO-66-NH$_2$ for TNP detection. (a) Comparing the detection performance of different explosives (concentrations are all 10^{-10} g mL^{-1}). (b) Testing of explosives in the actual environment (soil and cloth). (c) Comparison with the LOD of the reported sensors in the literature.[10,12,39–52]

detection performance is worst and the relative change of currents is only 0.25 (Fig. 3c and f). Besides, AAO@UiO-66-NH$_2$ without a barrier layer is selected as a sensor to detect TNP under the same experimental conditions (Fig. 3g). The current changes are not conspicuous and are far less than those of AAO@UiO-66-NH$_2$ with barrier layers (Fig. 3h). At last, the effect of incubation position on detection performance is also researched, with separate incubation on the porous and barrier side, and subsequent transmembrane current detection (Fig. 3i). When incubating on the porous side, the current change is small and the relative change is only 0.2.

Application feasibility of the nanofluidic sensor

In practical explosives detection scenarios, a variety of explosives would disturb the detection performance of TNP. Fig. 4a illustrates the relative change of current of AAO@UiO-66-NH$_2$ after detecting prevalent explosives, including hexogen (RDX), diazodinitrophenol (DDNP), 2,4,6-trinitrotoluene (TNT), octogen (HMX), and pentaerythritol tetranitrate (PETN). Compared with the other explosives, the currents of TNP exhibit more pronounced current signal changes. Outstanding selectivity indicates the specificity of the sensor, which effectively avoids false positives. The application feasibility of the nanofluidic sensor is evaluated in the actual environment. The samples collected from soil and cloth containing TNP are tested to evaluate the actual detection performance for TNP. The result exhibits that TNP could be selectively detected in samples from the actual environment (Fig. 4b). Stable current and tiny relative change of current over time indicate that the sensor could maintain long-term reliability (Fig. S17†). Notably, the limit of detection (LOD) of AAO@UiO-66-NH$_2$ is lower than some reported detection methods, including a variety of detection methods, such as fluorescence quenching, electrochemical, aggregation induced emission and other methods (Fig. 4c). The nanofluidic sensor with good sensitivity and selectivity anticipates broad application viability.

Conclusion

In summary, an OSNs-inspired nanofluidic sensor is devised to ultrasensitively detect TNP. The target molecule could be specifically captured by AAO@UiO-66-NH$_2$ through electrostatic and hydrogen bonding interactions and forms Meisenheimer complexes with amino groups on the framework. The steric hindrance and zeta potential are regulated after capturing targets, which combines to affect the ion transport across the membrane. This nanofluidic sensor enables detection of TNP in the concentration range of 10^{-14} to 10^{-10} g mL^{-1} and has an ultra-low limit of detection of 6.5×10^{-16} g mL^{-1}, making it one of the most advanced sensors in the literature. This work has the potential to trigger further scientific explorations in the design of sensors for trace target analysis, and provide significant guidance for other explosives detection in homeland security, military applications, security inspections and environmental monitoring.

Data availability

The data supporting the findings can be found in the article and ESI,† and are available from the authors upon reasonable request.

Author contributions

Xin Li: conceptualization, methodology, writing – original draft, writing – review & editing, visualization, validation, formal analysis, investigation, resources, and data curation. Zhanfang Liu: resources and investigation. Linsen Yang: investigation and formal analysis. Shengyang Zhou: investigation and resources. Yongchao Qian: methodology and resources. Yuge Wu: investigation and visualization. Zidi Yan: software. Zhehua Zhang: investigation and resources. Tingyang Li: investigation and resources. Qingchen Wang: investigation and resources. Congcong Zhu: investigation, writing – review & editing and resources. Xiang-Yu Kong: investigation, supervision and resources. Liping Wen: conceptualization, supervision and project administration.

Conflicts of interest

There are no conflicts to declare.

Acknowledgements

References

1 J. H. Song and D. W. Kang, Hazardous nitroaromatic explosives detection by emerging porous solid sensors, *Coord. Chem. Rev.*, 2023, **492**, 215279.

2 K. C. To, S. Ben-Jaber and I. P. Parkin, Recent developments in the field of explosive trace detection, *ACS Nano*, 2020, **14**, 10804–10833.

3 Z. Hu, K. Tan, W. P. Lustig, H. Wang, Y. Zhao, C. Zheng, D. Banerjee, T. J. Emge, Y. J. Chabal and J. Li, Effective sensing of RDX via instant and selective detection of ketone vapors, *Chem. Sci.*, 2014, **5**, 4873–4877.

4 S. S. Nagarkar, B. Joarder, A. K. Chaudhari, S. Mukherjee and S. K. Ghosh, Highly selective detection of nitro explosives by a luminescent metal-organic framework, *Angew. Chem., Int. Ed.*, 2013, **52**, 2881–2885.

5 S. Shanmugaraju, C. Dabadie, K. Byrne, A. J. Savyasachi, D. Umadevi, W. Schmitt, J. A. Kitchen and T. Gunnlaugsson, A supramolecular Tröger's base derived coordination zinc polymer for fluorescent sensing of phenolic-nitroaromatic explosives in water, *Chem. Sci.*, 2017, **8**, 1535–1546.

6 Y. Engel, R. Elnathan, A. Pevzner, G. Davidi, E. Flaxer and F. Patolsky, Supersensitive detection of explosives by

silicon nanowire arrays, *Angew. Chem., Int. Ed.*, 2010, **49**, 6830–6835.

7 M.-L. Hu, M. Joharian, S. A. A. Razavi, A. Morsali, D.-Z. Wu, A. Azhdari Tehrani, J. Wang, P. C. Junk and Z.-F. Guo, Phenolic nitroaromatics detection by fluorinated metal-organic frameworks: barrier elimination for selective sensing of specific group of nitroaromatics, *J. Hazard. Mater.*, 2021, **406**, 124501.

8 S. Wang, Q. Wang, X. Feng, B. Wang and L. Yang, Explosives in the cage: metal-organic frameworks for high-energy materials sensing and desensitization, *Adv. Mater.*, 2017, **29**, 1701898.

9 L. Guo, Z. Yang and X. Dou, Artificial olfactory system for trace identification of explosive vapors realized by optoelectronic Schottky sensing, *Adv. Mater.*, 2017, **29**, 1604528.

10 W. Liu, Z. Wang, Z. Liu, J. Chen, L. Shi, L. Huang, Y. Liu, S. Cui and X. He, Utilizing an automated SERS-digital microfluidic system for high-throughput detection of explosives, *ACS Sens.*, 2023, **8**, 1733–1741.

11 J. Y. Lee, H. D. Root, R. Ali, W. An, V. M. Lynch, S. Bahring, I. S. Kim, J. L. Sessler and J. S. Park, Ratiometric turn-on fluorophore displacement ensembles for nitroaromatic explosives detection, *J. Am. Chem. Soc.*, 2020, **142**, 19579–19587.

12 B. Wang, X.-L. Lv, D. Feng, L.-H. Xie, J. Zhang, M. Li, Y. Xie, J.-R. Li and H.-C. Zhou, Highly stable Zr(IV)-based metal–organic frameworks for the detection and removal of antibiotics and organic explosives in water, *J. Am. Chem. Soc.*, 2016, **138**, 6204–6216.

13 L. Bocquet, Nanofluidics coming of age, *Nat. Mater.*, 2020, **19**, 254–256.

14 Z. Zhang, L. Wen and L. Jiang, Nanofluidics for osmotic energy conversion, *Nat. Rev. Mater.*, 2021, **6**, 622–639.

15 Y. L. Ying, Z. L. Hu, S. Zhang, Y. Qing, A. Fragasso, G. Maglia, A. Meller, H. Bayley, C. Dekker and Y. T. Long, Nanopore-based technologies beyond DNA sequencing, *Nat. Nanotechnol.*, 2022, **17**, 1136–1146.

16 G. Laucirica, Y. Toum Terrones, V. Cayón, M. L. Cortez, M. E. Toimil-Molares, C. Trautmann, W. Marmisollé and O. Azzaroni, Biomimetic solid-state nanochannels for chemical and biological sensing applications, *TrAC, Trends Anal. Chem.*, 2021, **144**, 116425.

17 A. Soozanipour, H. Sohrabi, F. Abazar, A. Khataee, A. Noorbakhsh, M. Asadnia, A. Taheri-Kafrani, M. R. Majidi and A. Razmjou, Ion selective nanochannels: from critical principles to sensing and biosensing applications, *Adv. Mater. Technol.*, 2021, **6**, 2000765.

18 L. Yang, X.-Y. Kong and L. Wen, Bio-inspired nano-/micro-channels via supramolecular assembling: from fundamentals to applications, *Supramol. Mater.*, 2023, **2**, 100043.

19 H. Niu, M.-Y. Li, Y.-L. Ying and Y.-T. Long, An engineered third electrostatic constriction of aerolysin to manipulate heterogeneously charged peptide transport, *Chem. Sci.*, 2022, **13**, 2456–2461.

20 Y. Liu, Y. Qian, L. Fu, C. Zhu, X. Li, Q. Wang, H. Ling, H. Du, S. Zhou, X.-Y. Kong, L. Jiang and L. Wen, Archaea-inspired switchable nanochannels for on-demand lithium detection by pH activation, *ACS Cent. Sci.*, 2024, **10**, 469–476.

21 Y. Qian, Z. Zhang, X.-Y. Kong, W. Tian, L. Wen and L. Jiang, Engineered artificial nanochannels for nitrite ion harmless conversion, *ACS Appl. Mater. Interfaces*, 2018, **10**, 30852–30859.

22 X. Q. Ran, H.-L. Qian and X.-P. Yan, Integrating ordered two-dimensional covalent organic frameworks to solid-state nanofluidic channels for ultrafast and sensitive detection of mercury, *Anal. Chem.*, 2022, **94**, 8533–8538.

23 D. Zhang, Y. Sun, Z. Wang, F. Liu and X. Zhang, Switchable biomimetic nanochannels for on-demand SO_2 detection by light-controlled photochromism, *Nat. Commun.*, 2023, **14**, 1901.

24 X. Shang, G. Xie, X.-Y. Kong, Z. Zhang, Y. Zhang, W. Tian, L. Wen and L. Jiang, An artificial CO_2-driven ionic gate inspired by olfactory sensory neurons in mosquitoes, *Adv. Mater.*, 2016, **29**, 1603884.

25 J. Guo, X. Liu, J. Zhao, H. Xu, Z. Gao, Z.-Q. Wu and Y.-Y. Song, Rational design of mesoporous chiral MOFs as reactive pockets in nanochannels for enzyme-free identification of monosaccharide enantiomers, *Chem. Sci.*, 2023, **14**, 1742–1751.

26 X. Li, L. Yang, S. Zhou, Y. Qian, Y. Wu, X. He, W. Chen, Z. Zhang, T. Li, Q. Wang, C. Zhu, X. Y. Kong and L. Wen, Neuron-inspired nanofluidic biosensors for highly sensitive and selective imidacloprid detection, *ACS Sens.*, 2023, **8**, 3428–3434.

27 D. Meng, C. Hao, J. Cai, W. Ma, C. Chen, C. Xu, L. Xu and H. Kuang, Tailored chiral copper selenide nanochannels for ultrasensitive enantioselective recognition and detection, *Angew. Chem., Int. Ed.*, 2021, **60**, 24997–25004.

28 Z. Chen, Z. Wang, Y. Xu, X. Zhang, B. Tian and J. Bai, Controlled movement of ssDNA conjugated peptide through Mycobacterium smegmatis porin A (MspA) nanopore by a helicase motor for peptide sequencing application, *Chem. Sci.*, 2021, **12**, 15750–15756.

29 W. Liu, Z.-L. Yang, C.-N. Yang, Y.-L. Ying and Y.-T. Long, Profiling single-molecule reaction kinetics under nanopore confinement, *Chem. Sci.*, 2022, **13**, 4109–4114.

30 R.-J. Yu, S.-M. Lu, S.-W. Xu, Y.-J. Li, Q. Xu, Y.-L. Ying and Y.-T. Long, Single molecule sensing of amyloid-β aggregation by confined glass nanopores, *Chem. Sci.*, 2019, **10**, 10728–10732.

31 L.-L. Zhang, C.-B. Zhong, T.-J. Huang, L.-M. Zhang, F. Yan and Y.-L. Ying, High-throughput single biomarker identification using droplet nanopore, *Chem. Sci.*, 2024, **15**, 8355–8362.

32 X. P. Zhao, F. F. Liu, W. C. Hu, M. R. Younis, C. Wang and X. H. Xia, Biomimetic nanochannel-ionchannel hybrid for ultrasensitive and label-free detection of microRNA in cells, *Anal. Chem.*, 2019, **91**, 3582–3589.

33 J. Jiang, M. Y. Li, X. Y. Wu, Y. L. Ying, H. X. Han and Y. T. Long, Protein nanopore reveals the renin-angiotensin

system crosstalk with single-amino-acid resolution, *Nat. Chem.*, 2023, **15**, 578–586.

34 M. Woellner, S. Hausdorf, N. Klein, P. Mueller, M. W. Smith and S. Kaskel, Adsorption and detection of hazardous trace gases by metal-organic frameworks, *Adv. Mater.*, 2018, **30**, 1704679.

35 X. Zhang, S. Chen, S. Jin, Y. Zhang, X. Chen, Z. Zhang and Q. Shu, Naphthalene based lab-on-a-molecule for fluorimetric and colorimetric sensing of F^- and CN^- and nitroaromatic explosives, *Sens. Actuators, B*, 2017, **242**, 944–998.

36 X. Liu, Y. Han, Y. Shu, J. Wang and H. Qiu, Fabrication and application of 2,4,6-trinitrophenol sensors based on fluorescent functional materials, *J. Hazard. Mater.*, 2022, **425**, 127987.

37 Q. Sun, Z. Wu, Z. Qin, X. Chen, C. Zhang, B. Cao, H. Duan and J. Zhang, A dog nose-inspired high-performance NH_3 gas sensor of biomass carbon materials with a pleated structure derived from rose tea, *J. Mater. Chem. A*, 2022, **10**, 14326–14335.

38 S. Firestein, How the olfactory system makes sense of scents, *Nature*, 2001, **413**, 211–218.

39 A. Chatz-Giachia, A. E. Psalti, A. D. Pournara, M. J. Manos, C. Pappa, K. Triantafyllidis and T. Lazarides, Detection of nitrophenols with a fluorescent Zr(IV) metal–organic framework functionalized with benzylamino groups, *J. Mater. Chem. C*, 2022, **10**, 12307–12315.

40 L. Havlíková, R. Matyáš, L. Ihnát, L. Nováková and D. Šatínský, Degradation study of nitroaromatic explosives 2-diazo-4,6-dinitrophenol and picramic acid using HPLC and UHPLC-ESI-MS/MS, *Anal. Methods*, 2014, **6**, 4761–4768.

41 N. A. Khan, S. Waheed, H. M. Junaid, A. Hamad, M. Imran, S. H. Shah, G. S. Khan and S. A. Shahzad, Ultra-sensitive fluorescent and colorimetric probes for femtomolar detection of picric acid: mechanochromic, latent fingerprinting, and pH responsive character with AIE properties, *J. Photochem. Photobiol., A*, 2023, **435**, 114318.

42 A. Kumar and P. S. Chae, New 1,8-naphthalimide-conjugated sulfonamide probes for TNP sensing in water, *Sens. Actuators, B*, 2017, **240**, 1–9.

43 A. Kumar and P. S. Chae, Aggregation induced emission enhancement behavior of conformationally rigid pyreneamide-based probe for ultra-trace detection of picric acid (PA), *Dyes Pigm.*, 2018, **156**, 307–317.

44 A. Kumar, A. Pandith and H.-S. Kim, Pyrene-appended imidazolium probe for 2,4,6-trinitrophenol in water, *Sens. Actuators, B*, 2016, **231**, 293–301.

45 A. Ramachandran, J. S. Arya Nair and S. Karunakaran Yesodha, Polyaniline-derived nitrogen-doped graphene quantum dots for the ultratrace level electrochemical detection of trinitrophenol and the effective differentiation of nitroaromatics: structure matters, *ACS Sustainable Chem. Eng.*, 2019, **7**, 6732–6743.

46 A. Rawat, D. B. Kanzariya, P. Lama and T. K. Pal, Colorimetric response and real-field recognition of organo-toxins and antibiotics in aqueous medium using a 2D coordination polymer, *Cryst. Growth Des.*, 2023, **23**, 7763–7776.

47 A. Riaz, S. u. Din, A. Rakha, N. A. Shad, A. Munawar and M. H. Siddiqi, Harnessing MoS_2 nanomaterials for TNP sensing and anticancer efficacy, *Mater. Chem. Phys.*, 2024, **312**, 128619.

48 D. Sangamithirai and S. Ramanathan, Electrochemical sensing platform for the detection of nitroaromatics using $g-C_3N_4/V_2O_5$ nanocomposites modified glassy carbon electrode, *Electrochim. Acta*, 2022, **434**, 141308.

49 H. Şener, B. Anilanmert and S. Cengiz, A fast method for monitoring of organic explosives in soil: a gas temperature gradient approach in LC–APCI/MS/MS, *Chem. Pap.*, 2017, **71**, 971–979.

50 N. Tripathi, S. Sandhu, P. Singh, A. Mahajan, M. Kaur and S. Kumar, Dansyl conjugated tripodal AIEEgen for highly selective detection of 2,4,6-trinitrophenol in water and solid state, *Sens. Actuators, B*, 2016, **231**, 79–87.

51 K. Xing, R. Fan, J. Wang, S. Zhang, K. Feng, X. Du, Y. Song, P. Wang and Y. Yang, Highly stable and regenerative metal–organic framework designed by multiwalled divider installation strategy for detection of Co(II) ions and organic aromatics in water, *ACS Appl. Mater. Interfaces*, 2017, **9**, 19881–19893.

52 C. Zheng, Y. Ling, J. Chen, X. Yuan, S. Li and Z. Zhang, Design of a versatile and selective electrochemical sensor based on dummy molecularly imprinted PEDOT/laser-induced graphene for nitroaromatic explosives detection, *Environ. Res.*, 2023, **236**, 116769.